Programming characteristics of electrochemical random-access memory (ECRAM) - Part II: Physics-based Modeling

M. Porzani, *Graduate Student Member, IEEE*, F. Carletti, *Graduate Student Member, IEEE*, S. Ricci, M. Farronato, *Member, IEEE*, D. Ielmini, *Fellow, IEEE*

***Abstract*— Modeling of electrochemical random-access memory (ECRAM) is essential to predict device performance and scaling, and provide simulation tools for in-memory computing (IMC) circuits. This paper addresses physical modeling of ECRAM capable of describing both the quasi-static characteristics and the pulsed programming dynamics of the device. Channel potentiation and depression are described in terms of nonlinear drift-diffusion of mobile oxygen vacancies in the layers of the device. An analytical compact model for pulsed channel potentiation is derived from the physical picture to support circuit simulations. Simulation results are extensively compared with experimental data. The model accounts for device potentiation characteristics and accurately describes second-order effects such as saturation and nonlinearity deviations.**

***Index Terms*— ECRAM, emerging memory technologies, oxygen vacancy, physical modeling, resistive memory.**

I. Introduction

The electrochemical random-access memory (ECRAM) is a three-terminal resistive memory that is gaining popularity for in-memory computing (IMC) applications [1] thanks to its linear and reproducible conductance update curves, low power and scalability. Fig. 1 shows the vertical cross-section of the device consisting of a tungsten oxide WO_x channel contacted by two source and drain metal electrodes. On top of the channel there is a gate stack composed of an electrolyte layer, a reservoir layer and a gate metal layer. ECRAM operation relies on modulating the oxygen vacancy concentration in the channel to achieve resistive switching. This effect is achieved with gate voltage application, as the electric fields developed inside the device enable fast migration of oxygen vacancies across the electrolyte layer, allowing channel ion injection/extraction. In the companion paper [2] we demonstrated that, when a triangular voltage sweep is applied at the gate, the ECRAM exhibits orders of magnitude of channel conductance modulation with a wide counterclockwise I_D current hysteresis and an associated clockwise ionic gate current loop as shown in Fig. 2(a) and (b). We also demonstrated a precise linear channel conductance update following the application of a positive gate pulse of amplitude $+V$ and short duration t_p, as shown in Fig. 2(c). To account for these experimental features, it is essential to develop a physics-based model that can support the device engineering as well as to better understand the role of oxygen vacancy and device optimization.

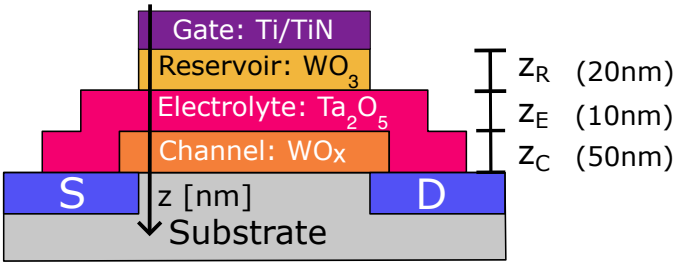

Fig. 1. Schematic vertical cross-section of an ECRAM device. The 1-D model considered in this analysis refers to the z coordinate axis shown in figure. The thicknesses shown in figure correspond to the physical prototypes fabricated and measured for this analysis.

This paper presents a physical model for ECRAMs based on oxygen vacancy migration and nonlinear conductance modulation. An analytical closed formula is derived to precisely describe linear ΔG channel update and compared to experimental data reported in the companion paper [2]. Simulation results provide an accurate, quantitative description of both large hysteresis and linear weight update. The model can be used for device and circuit simulations, thus supporting the design-technology co-optimization (DTCO) of ECRAM-based IMC circuits.

II. Physical Modeling

We will consider a one-dimensional (1D) model for the ECRAM device along the vertical z-axis (see Fig. 1) crossing the three metal-oxide regions in contact, namely reservoir, electrolyte and channel layers. We will assume a sub-stoichiometric oxide composition, with a large concentration of oxygen vacancies (V_o) that are able to migrate and modulate the channel conductance. As shown schematically in Fig. 1 the reference coordinate z axis is taken orthogonal to the channel, with the thickness of the reservoir, electrolyte and

Submitted for review on 18/12/2023. This work received funding from ECSEL Joint Undertaking (JU) under grant agreement no. 101007321. The JU receives support from the European Union's Horizon 2020 research and innovation programme and France, Belgium, Czech Republic, Germany, Italy, Sweden, Switzerland, Turkey.

M. Porzani, F. Carletti, S. Ricci, M. Farronato and D. Ielmini are with the Dipartimento di Elettronica, Informazione e Bioingegneria, Politecnico di Milano, 20133 Milan, Italy (e-mail: daniele.ielmini@polimi.it).

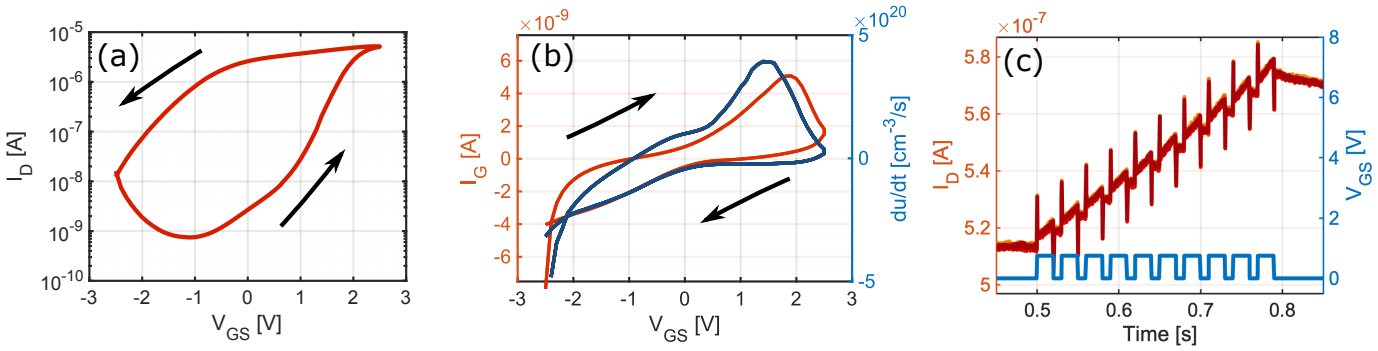

Fig. 2. Experimental measurements of ECRAM devices under different working regimes. (a) Large signal channel current I_D and (b) Comparison between gate current I_G for a 60 s gate sweep transcharacteristic, measured with V_{DS} = 0.1 V and du/dt derived from I_D via Eq. (1). (c) Small signal channel potentiation measured for the application of a train of ten gate voltage pulses with $20\,ms$ pulsewidth and 1.5 V amplitude.

channel layer respectively taken as z_R, z_E and z_C. The top boundary represents the gate contact, while the bottom boundary represents the channel electrical ground reference. Oxygen ions are not allowed to escape from the boundaries, thus the total number of oxygen vacancies is conserved within the simulated domain during device operation.

Optimal device operation relies on the ideal properties of each of the functional layers [3], [4]. The electrolyte layer, which acts as a barrier between reservoir and channel, should have a high ionic conductivity as well as high electronic resistivity, to allow for both large potential drop across the layer and efficient vacancy transport induced by electric field [5]. A high channel ionic diffusivity is crucial to allow for fast redistribution of the defects injected into the channel. Finally, the reservoir should be both able to provide ions during channel potentiation and to store excess ions during channel depression, to support a large on/off ratio of the device conductance G.

WO_3 is a transition-metal oxide vastly used as channel material in ECRAM devices for its electronic properties [4]–[8]. Sub-stoichiometric WO_x films are highly sensitive to oxygen content and exhibit a steep insulator-to-semiconductor transition with varying oxygen vacancy concentration [9]–[11]. By observing the experimental relation between channel conductance and injected gate charge (Fig. 3 in the companion paper [2]), we assumed that the WO_x electrical conductivity σ follows the formula:

$$\sigma(u) = Be^{u/u_0} \tag{1}$$

where u $[cm^{-3}]$ is the concentration of oxygen vacancies in the material, u_0 a constant, and B a pre-exponential coefficient reported in Tab. I.

The electrical conduction obeys to the carrier continuity equation:

$$\nabla \cdot \sigma \nabla \psi = 0 \tag{2}$$

where ψ is the local electrostatic potential and σ is either given by Eq. (1) in the channel and reservoir region, or is assumed equal to a constant value σ_0 in the electrolyte layer as reported in Tab. I.

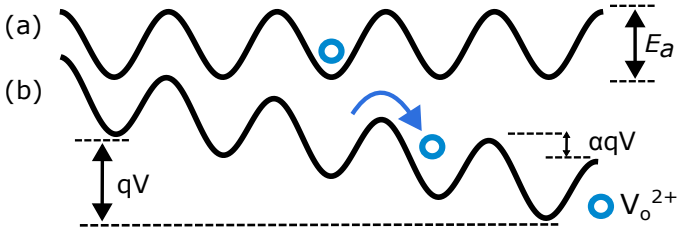

Fig. 3. Schematic of the potential energy profile for ion hopping at (a) zero or (b) positive applied voltage. The barrier lowering seen by a vacancy in a potential well is proportional to the applied voltage.

Since device operation is based on modulating V_o concentration to update the channel conductance, we adopted a model for ion migration based on thermally-assisted ion-hopping. Fig. 3 shows the oxygen vacancy in a spatial profile of potential wells with energy barrier E_a and with uniform spacing Δz [12]. An oxygen vacancy with sufficient thermal energy is able to move from one lattice site to another by overcoming the energy barrier. By considering the statistical ensemble of oxygen vacancies in the material and the Maxwell-Boltzmann distribution, vacancies diffuse isotropically with a rate proportional to the concentration gradient [12], [13]. The diffusive flux $[cm^{-2}s^{-1}]$ can be described by Fick's first law:

$$J_{diff} = -D_0 e^{-E_a/k_B T} \frac{\partial u}{\partial x} = -D \frac{\partial u}{\partial x} \tag{3}$$

where D_0 is a diffusivity coefficient, k_B and T are Boltzmann constant and the local temperature respectively. D $[cm^2 s^{-1}]$ is the material-dependent ionic diffusivity for oxygen vacancies, thermally activated with an Arrhenius law. The D used in the model are reported in Table I. We chose for simplicity the same E_a in all materials, without compromising the generality of the results.

The application of an external electric field $F = -\nabla\psi$, decreases the energy barrier in Fig. 3 according to:

$$\Delta E = ZqF\Delta z/2, \tag{4}$$

where $Z = 2$ is the charge number of the mobile vacancy and q the elementary charge [14]. Oxygen vacancy migration is exponentially enhanced via ion hopping, with a net average

drift velocity in the direction of the field. The drift flux can be modeled by [12], [14], [15]:

$$J_{drift} = \nu_0 e^{-E_a/k_B T} \Delta z \sinh\left(ZqF\frac{\Delta z}{2k_B T}\right) u \qquad (5)$$

where ν_0 is the frequency of escape attempts, reported in Tab. I.

The time evolution of the oxygen vacancy concentration u is described by the drift-diffusion transport equation:

$$\frac{\partial u}{\partial t} = -\frac{\partial}{\partial x}(J_{diff} + J_{drift}) \qquad (6)$$

that considers ionic fluxes arising either by an external electric field or by diffusion. In our ECRAM model, the coefficients for both drift and diffusion are material dependent.

Eq. (6) is coupled through the electrostatic potential ψ with Eq. (2), while at the same time dictating the time evolution of channel conductivity in Eq. (1). The coupled system of three equations will be used to model both large signal and small signal behavior of the ECRAM. In the model the interfaces between the materials are simply described as step discontinuities of their physical coefficients, neglecting more nuanced effects such as localized states.

The model can in principle be extended to ECRAM devices relying on other types of migrating ions [4], [16], provided that the physical coefficients (such as the ionic diffusivity), the ionic charge number Z, and the relationship between the defect concentration in the channel and the channel conductivity are appropriately modified to account for the different ionic species.

III. Analytical Modeling

Starting from the physical picture in Eqs. (1) - (6), it is possible to derive an analytical compact formula for ECRAM channel potentiation in the particular case of a short gate voltage pulse of amplitude V and time duration t_p. Fig. 4 shows the calculated electrostatic potential profile across the device during gate voltage application. Given the high resistivity of the electrolyte layer, most of the potential drop will fall across the electrolyte with an uniform electric field $F = V/z_E$. Based on the nonlinear voltage dependence of ion-hopping in (5), the total oxygen vacancy flux J_u in the electrolyte layer can thus be attributed to drift according to the formula:

$$J_u \simeq J_{drift} = A \sinh\left(\alpha \frac{qV}{k_B T}\right) \qquad (7)$$

where coefficients $A = 5.47 \times 10^{18}\, cm^{-2}s^{-1}$ and $\alpha = 0.046$ were extracted from experimental measurements [2]. If the pulse duration t_p is short enough, no significant change in vacancy concentration occurs during the programming event, thus the flux can be considered constant. Saturation and back-diffusion phenomena can be neglected in this small injection regime.

This approach allows to decouple the problem as shown schematically in Fig. 4. Given the negligible electric fields in the channel, we can assume that the transport of defects is

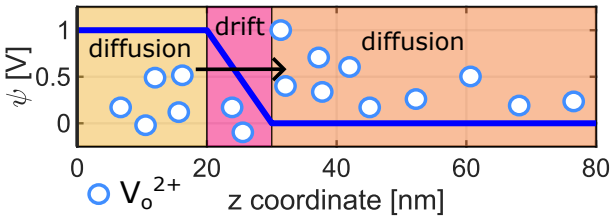

Fig. 4. Calculated electrostatic potential ψ, for a 1 V gate voltage application. The potential drops mainly over the electrolyte layer given its high resistivity.

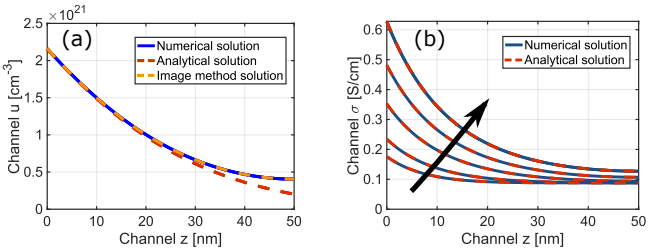

Fig. 5. (a) Comparison between numerically calculated u profile in the channel at a single time instant, analytical solution (11) and image method solution (12). (b) Comparison between numerically calculated and analytical σ in the channel, for increasing time.

mainly diffusive, thus Eq. (6) reduces to a diffusion equation problem with constant flux injection (Neumann boundary conditions) in the channel. Given the 1D geometry of the model, the diffusion equation is solved in the interval $[0; z_C]$. Since the solution resulting from the diffusion of an instantaneous point mass Q is known from mathematical analysis [17],

$$u(z,t) = \frac{Q}{\sqrt{4\pi D t}} \exp\left(\frac{-z^2}{4Dt}\right) \qquad (8)$$

a concentration distribution resulting from a specified mass rate injection, i.e. a flux, can be derived. A continuous flux is equivalent to the injection of a mass $J\delta t$ for each δt time increment. The concentration profile will result from the superposition of all the masses injected at all times before observation, given by:

$$u(z,t) = \int_{-\infty}^{t} \frac{J_u(\tau)}{\sqrt{4\pi D(t-\tau)}} \exp\left[\frac{-z^2}{4D(t-\tau)}\right] d\tau + u_i \qquad (9)$$

which is an integral solution in the form of a convolution with the Green's function. In the case of a general flux varying in time, Eq. (9) has to be computed numerically. In the case of

TABLE I
SIMULATION PARAMETERS

Parameter	WO_3 (channel)	Ta_2O_5	WO_3 (reservoir)
$u_0\ [cm^{-3}]$	8×10^{20}	-	8×10^{20}
$B\ [\Omega^{-1}cm^{-1}]$	5.93×10^{-4}	-	5.93×10^{-4}
$D\ [cm^2 s^{-1}]$	1.09×10^{-12}	8.24×10^{-14}	8.24×10^{-12}
$E_a\ [eV]$	0.2924		
$\Delta z\ [nm]$	0.46		
$\sigma_0\ [\Omega^{-1}cm^{-1}]$	8.8×10^{-2}	5×10^{-9}	8.8×10^{-2}
$\nu_0\ [s^{-1}]$	1.2136×10^{9}	1.2136×10^{6}	1.2136×10^{9}
$u_i\ [cm^{-3}]$	4×10^{21}		

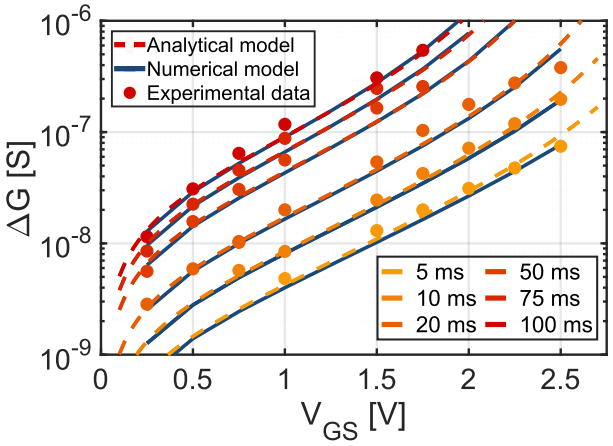

Fig. 6. Comparison between analytical ΔG calculated with (14), ΔG extracted from experimental measurements and numerically calculated ΔG as a function of V_{GS} pulse amplitude and t_p duration.

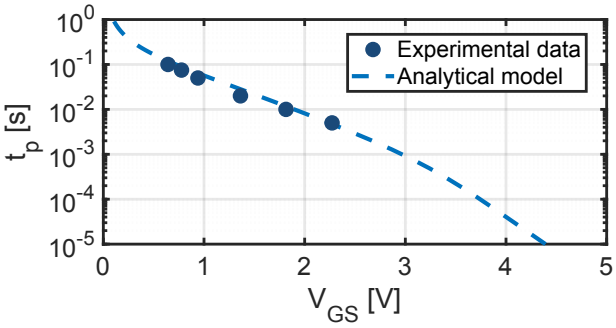

Fig. 7. Pulse time needed to achieve a ΔG modulation of 5×10^{-8} S as a function of pulse amplitude. The interpolated experimental data from Fig. 6, is compared to the analytical model.

a constant J injection into the channel, however, the equation can be solved analytically. By assuming that the flux injection at $x = 0$ starts at $t = 0$, we can write concentration difference $\Delta u(z,t) = u(z,t) - u_i$ as:

$$\Delta u(z,t) = \frac{J_u}{\sqrt{4\pi D}} \int_0^t \frac{1}{\sqrt{(t-\tau)}} \exp\left[\frac{-z^2}{4D(t-\tau)}\right] d\tau. \tag{10}$$

Eq. (10) can be solved by substitution technique, with the primitive being the incomplete gamma function $\Gamma(a,x)$ [18]. Note that vacancies diffuse towards both $z > 0$ and $z < 0$, thus the solution of Eq. (10) solution is symmetric. To recover the vacancies diffused to negative z, an additional factor 2 is needed in the solution, resulting in

$$\Delta u(z,t) = 2J_u\sqrt{\frac{t}{D\pi}} \exp\left[\frac{-z^2}{4Dt}\right] - J_u \frac{z}{D} \operatorname{erfc}\left(\frac{z}{\sqrt{4Dt}}\right) \tag{11}$$

with erfc being the complementary error function.

Eq. (11) describes the diffusion of V_o in the channel also for $z > z_C$. To implement a zero-flux boundary condition at the channel interface with the substrate, we will consider the image-method equation [19]:

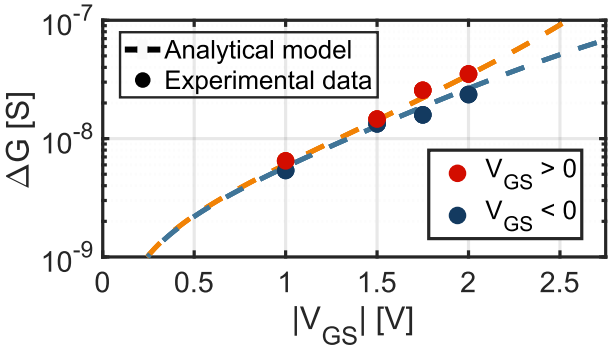

Fig. 8. Experimental median ΔG as a function of absolute V_{GS} for both potentiation (positive) and depression (negative) pulses with t_p = 10 ms compared to the analytical compact model, that captures the asymmetry of ΔG programming.

$$\Delta \bar{u}(z,t) = \Delta u(z,t) + \Delta u(2z_C - z, t) \tag{12}$$

which prevents the out-diffusion from the bottom boundary, thus preserving the total number of injected vacancies in the channel. Eq. (12) thus provides the increase in the concentration profile of oxygen vacancies in the channel upon a constant injection from the electrolyte side. Fig.5(a) shows a comparison between the image correction in Eq. (12) and the numerical solution calculated with the numerical model, indicating a close agreement between the two simulation results. The results of the analytical Eq. (11) are also reported, showing the inaccurate description of concentration profile at the bottom channel boundary.

The concentration profile in the channel can be used to calculate the conductivity according to Eq. (1), equivalently expressed in terms of Δu as:

$$\sigma(z,t) = \sigma_0 \exp\left(\frac{\Delta \bar{u}(z,t)}{u_0}\right) \tag{13}$$

with σ_0 the initial conductivity. Fig 5(b) shows a comparison between σ calculated numerically and analytically with Eq. (13). Finally, channel conductance G is calculated by integrating the local conductivity across the channel depth according to:

$$G(t) = \frac{W}{L}\sigma_0 \int_0^{z_C} \exp\left(\frac{\Delta \bar{u}(z,t)}{u_0}\right) dz \tag{14}$$

where W and L are the width and length of the channel, respectively. D introduces a time dynamic in the evolution of G. For times longer than the characteristic time of diffusion $t_d = z_C^2/D$ there is a noticeable redistribution of vacancies along the channel length [17], with a corresponding averaging of the injected defects which affects the overall G.

To validate (14), Fig.6 shows the measured and calculated ΔG, namely the change of conductance after the application of a pulse with gate voltage V and width t_p. The results indicate that ΔG shows a highly non-linear increase with V_{GS}, which can be explained by the non-linear dependence in Eqs. (7) and (13). As a consequence of this fast programming times can be obtained for high V_{GS} [15]. Fig. 7 shows the

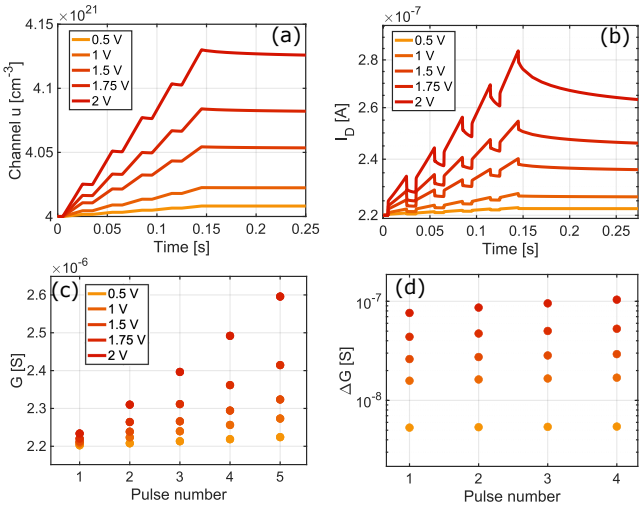

Fig. 9. Numerical simulation results. (a) Channel average concentration $\boldsymbol{u}$. (b) Channel current $\boldsymbol{I_D}$. (c) $\boldsymbol{G}$ and (d) $\boldsymbol{\Delta G}$ for a five pulses gate voltage sequence. Pulse duration is $\boldsymbol{t_p} = 20$ ms with 10 ms between each pulse, and $\boldsymbol{V_{GS}}$ varies from 0.5 to 2 V.

measured and calculated t_p needed to reach a ΔG modulation of 5×10^{-8} S as a function of the gate voltage. The results indicate that the programming time decreases exponentially for increasing pulse amplitude in the medium voltage regime. The compact model is able to provide an accurate description of ΔG over more than two decades of conductance. At low voltages $V < 0.75\,V$ the model captures deviation from the exponential trend due to the hyperbolic sine in Eq. (5).

The model also applies to device depression, as a negative V_{GS} reverses the electric field direction across the electrolyte and allows extraction of defects from the channel. Fig. 8 shows measured ΔG for V_{GS} of both polarities compared to analytical ΔG calculated with Eq. (14). As a result of the non-linearity of Eq. (13), ΔG predicted by the model is intrinsically not symmetrical for negative V_{GS} polarity, with lower absolute ΔG for depression, and as such captures the asymmetry between potentiation and depression observed experimentally. For the model of this device all coefficients were taken from Tab I, while $\alpha = 0.041$ was extracted from data.

IV. Numerical Modeling

To support and validate the compact model of ECRAM, we also developed a numerical model of ECRAM consisting of the numerical solution of the transport equation for oxygen vacancies (6), the current continuity equation for electronic conduction (2) and the conductivity equation (1). This system of coupled partial differential equations is solved using a numerical solver, namely COMSOL Multiphysics ® [20], to investigate the effect of arbitrary gate voltage inputs. The equations are solved on a one dimensional geometry having the same dimensions as the fabricated samples in consideration.

With respect to the compact model, the numerical model can capture more physical details such as the saturation and other effects that were neglected by the analytical compact model. The solution of the 1-D model with the appropriate boundary

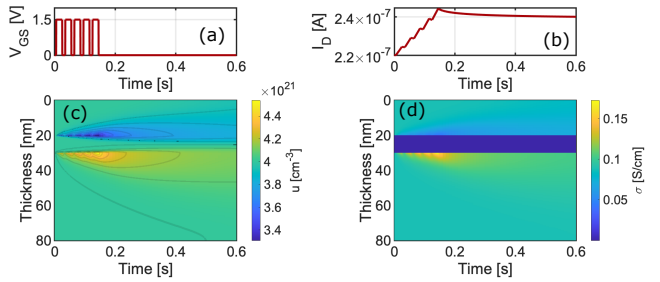

Fig. 10. Numerical simulation of a pulsed gate voltage experiment consisting in a sequence of five pulses of 20 ms duration and 1.5 V amplitude. (a) Applied $\boldsymbol{V_{GS}}$ waveform. (b) Calculated $\boldsymbol{I_D}$. Calculated (c) $\boldsymbol{u}$ and (d) $\boldsymbol{\sigma}$ as a function of time in the device.

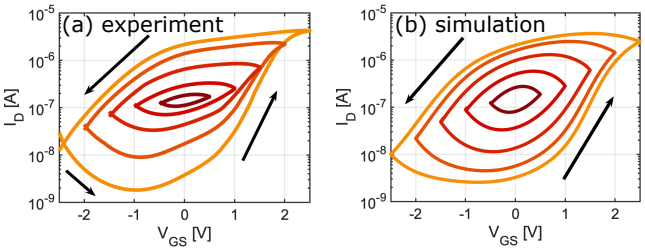

Fig. 11. (a) Experimentally measured and (b) numerically simulated channel hysteresis $\boldsymbol{I_D}$ curve characteristics for different gate voltage amplitudes, obtained by applying triangular gate voltage sweeps of 60 s total time ramp duration.

conditions allows to calculate u, J_u and ψ as a function of time within the device. The conductivity modulation is provided by the solver via Eq. (1). The temperature was assumed constant at $T = 300\,K$. The channel current is derived by applying Ohm's law to the channel, namely:

$$I_D(t) = G(t)V_{DS}, \tag{15}$$

where G is calculated by Eq. (14) assuming a channel area $W \times L = 50\mu m \times 10\mu m$ and thickness z_C. The drain voltage was set $V_{DS} = 0.1$ V as in the actual experiment. The gate current, which is due to ionic conduction in our model, can be derived from the total flux J_u of oxygen vacancies and their electrical charge Zq according to:

$$I_G(t) = ZqWLJ_u(t). \tag{16}$$

The electronic component of the gate current was neglected due to the high resistivity of the electrolyte layer.

Fig.9 shows the simulated (a) channel average u and (b) drain current for a sequence of five voltage pulses of duration $t_p = 20$ ms. The simulation also accounts for the ion contribution in the drain current waveform, which is estimated by summing I_D to $I_G/2$. With higher voltage pulse amplitude we observe a larger injection of vacancies in the channel, and correspondingly higher currents. A current decay of I_D can be observed when no gate voltage is applied. This can be explained by a combination of diffusion of the injected defects from the electrolyte-channel interface to the channel bulk, and diffusion from the channel layer back to the electrolyte.

The channel conductance G can be evaluated from a read pulse at low $V_{DS} = 0.1$ V after each pulse with $V_{GS} = 0$ V. Fig. 9(c) shows the calculated G as a function of the number of pulses for increasing V_{GS}. The channel conductance displays a high linearity which can also be appreciated from figure 9(d) where ΔG remains approximately constant with pulse number. For large pulse amplitude the conductance shows a significant non-linearity, which can be explained by the non-linear relationship between conductance and defect concentration in Eq. (13), as discussed in the companion paper [2].

Fig. 10 shows the simulated profile of (c) u and (d) σ as a function of time during programming operation with V_{GS} (a) applied. An initial oxygen vacancy concentration $u_i = 4 \times 10^{21}\,\mathrm{cm}^{-3}$ was assumed in all layers of the device. With each potentiation pulse, oxygen vacancies are injected in correspondence of the channel-electrolyte interface, in agreement with Eq. (12), while a corresponding depression is seen in the reservoir layer. The vacancy concentration in the electrolyte remains approximately constant, with a transfer of defects from the reservoir to the channel. Given the small injection of defects, the conductance change is still in a linear regime. For relatively long times, both diffusion of vacancies into the channel and back-diffusion in the electrolyte cause a decay of the current after the pulses, as shown in Fig. 9(b).

Fig. 6 shows the calculated channel ΔG as a function of V_{GS} for increasing programming time. The comparison between the numerical simulations, the results of the compact model and the experimental results show a good agreement, thus supporting the accuracy of the physical picture in the models.

Fig. 11 shows the measured (a) and simulated (b) I_D as a function of V_{GS} with a quasi-static voltage sweep. The simulations were performed assuming the same parameters (sweep rate and voltage range) of the experiment. The drain current I_D was sensed by application of a small $V_{DS} = 0.1$ V. The drain current displays a counterclockwise hysteresis where the current range increases with V_{GS} amplitude. The shape of the hysteresis curve is dictated by the interplay between injection of vacancies in the channel during positive V_{GS} sweep, and emission of vacancies during the negative V_{GS} sweep.

Fig. 12 shows the calculated (c) u and (d) σ as a function of time for a triangular V_{GS} sweep shown in (a). A large modulation of channel and reservoir vacancy concentration is seen, as the strong electric field induces the injection of a large amount of defects in the channel and the depletion in the reservoir layer. The channel conductivity σ follows a similar cyclical trend, although the modulation covers a few orders of magnitude as a result of the exponential dependence on u in Eq. (13). This modulation results in a large I_D hysteresis as shown in (b).

Fig.13 shows the measured (a) and calculated (b) I_G during the same V_{GS} sweeps of Fig. 11. The simulated current is purely ionic, according to Eq. (16), and scales with V_{GS} following a clockwise loop. The curves are closely related to I_D in Fig. 11, where the I_G peak is the signature of vacancy injection corresponding to the sharp increase in G. Indeed I_G can be linked to I_D by:

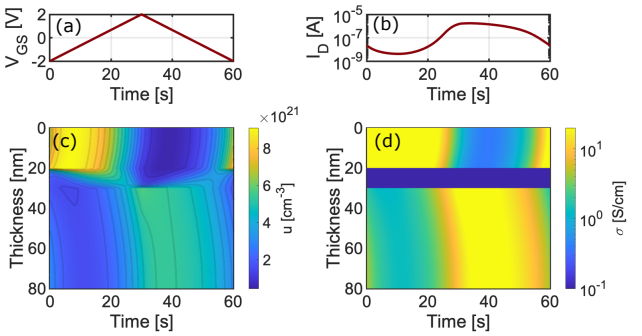

Fig. 12. Numerical simulation of a quasi-static gate voltage experiment consisting in a triangular gate voltage sweeps of 60 s total time ramp duration and 2 V amplitude. (a) Applied V_{GS} waveform. (b) Calculated I_D. Calculated (c) u and (d) σ as a function of time in the device.

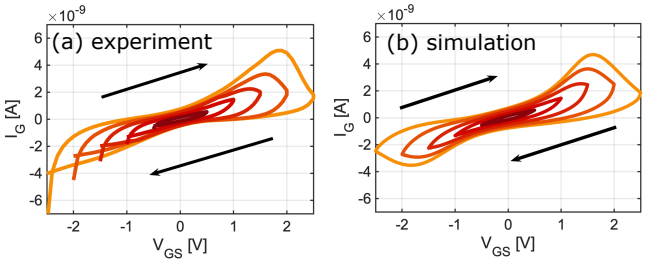

Fig. 13. (a) Experimentally measured and (b) numerically simulated gate current I_G curve characteristics for different gate voltage amplitudes, obtained by applying triangular gate voltage sweeps of 60 s total time ramp duration.

$$I_G(t) \propto \frac{du}{dt} \propto \frac{d}{dt} \log I_D(t). \tag{17}$$

To demonstrate this relationship we extracted u via Eq. (1) from the measured I_D in Fig. 2(a), and compared its time derivative to the measured I_G as shown in Fig. 2(b), indicating a very similar behavior, further supporting our interpretation. The asymmetric I_G hysteresis can be interpreted on the basis of different material parameters and physical dimensions of the channel and reservoir layers. Overall the simulation results can provide a quantitative description of all significant features of the electrical characteristics of the ECRAM device. The model thus provides a valuable simulation tool to support in-memory computing with ECRAM devices.

V. Conclusions

We presented a physical model for oxygen vacancy migration and conductance modulation in ECRAM devices capable of reproducing the device behavior under quasi-static sweeps and pulsed conductance programming. We derived an analytical compact model for ΔG potentiation following voltage pulse application with excellent agreement with experiments. A numerical model was then proposed to simulate the electrical characteristics under various experimental conditions. The model correctly describes I_D counterclockwise hysteresis, I_G clockwise behavior and pulsed channel potentiation, thus supporting the development of ECRAM in practical circuits.

REFERENCES

[1] P. Mannocci *et al.*, "In-memory computing with emerging memory devices: Status and outlook," *APL Machine Learning*, vol. 1, no. 1, p. 010902, Mar. 2023. doi: 10.1063/5.0136403

[2] M. Porzani *et al.*, "Programming characteristics of electrochemical random-access memory (ECRAM) - Part I: Experimental Study," *IEEE Trans. Electron Devices*, Submitted 2023.

[3] J. Lee *et al.*, "Strategies to Improve the Synaptic Characteristics of Oxygen-Based Electrochemical Random-Access Memory Based on Material Parameters Optimization," *ACS Appl. Mater. Interfaces*, vol. 14, no. 11, pp. 13 450–13 457, Mar. 2022. doi: 10.1021/acsami.1c21045

[4] A. A. Talin *et al.*, "ECRAM Materials, Devices, Circuits and Architectures: A Perspective," *Advanced Materials*, vol. 35, no. 37, p. 2204771, Sep. 2023. doi: 10.1002/adma.202204771

[5] Y. Jeong *et al.*, "Elucidating Ionic Programming Dynamics of Metal-Oxide Electrochemical Memory for Neuromorphic Computing," *Adv Elect Materials*, vol. 7, no. 8, p. 2100185, Aug. 2021. doi: 10.1002/aelm.202100185

[6] S. Kim *et al.*, "Metal-oxide based, CMOS-compatible ECRAM for Deep Learning Accelerator," in *2019 IEEE International Electron Devices Meeting (IEDM)*. San Francisco, CA, USA: IEEE, Dec. 2019, pp. 35.7.1–35.7.4. doi: 10.1109/IEDM19573.2019.8993463

[7] H. Kang *et al.*, "Ion-Driven Electrochemical Random-Access Memory-Based Synaptic Devices for Neuromorphic Computing Systems: A Mini-Review," *Micromachines*, vol. 13, no. 3, p. 453, Mar. 2022. doi: 10.3390/mi13030453

[8] P. M. Solomon *et al.*, "Transient Investigation of Metal-oxide based, CMOS-compatible ECRAM," in *2021 IEEE International Reliability Physics Symposium (IRPS)*. Monterey, CA, USA: IEEE, Mar. 2021, pp. 1–7. doi: 10.1109/IRPS46558.2021.9405156

[9] J. Lee *et al.*, "Improved Synaptic Characteristics of Oxide-Based Electrochemical Random Access Memory at Elevated Temperatures Using Integrated Micro-Heater," *IEEE Trans. Electron Devices*, vol. 69, no. 4, pp. 2218–2221, Apr. 2022. doi: 10.1109/TED.2022.3151306

[10] X. Zheng, "The influence of ion implantation-induced oxygen vacancy on electrical conductivity of WO3 thin films," *Vacuum*, vol. 165, pp. 46–50, Jul. 2019. doi: 10.1016/j.vacuum.2019.04.004

[11] J. Lee *et al.*, "Excellent synaptic behavior of lithium-based nano-ionic transistor based on optimal WO $_{2.7}$ stoichiometry with high ion diffusivity," *Nanotechnology*, vol. 31, no. 23, p. 235203, Mar. 2020. doi: 10.1088/1361-6528/ab793d

[12] N. F. Mott *et al.*, *Electronic processes in ionic crystals*, 2nd ed. New York: Dover, 1964, oCLC: 229912023.

[13] S. Larentis *et al.*, "Resistive Switching by Voltage-Driven Ion Migration in Bipolar RRAM—Part II: Modeling," *IEEE Trans. Electron Devices*, vol. 59, no. 9, pp. 2468–2475, Sep. 2012. doi: 10.1109/TED.2012.2202320

[14] D. Ielmini *et al.*, "Analytical model for subthreshold conduction and threshold switching in chalcogenide-based memory devices," *Journal of Applied Physics*, vol. 102, no. 5, p. 054517, Sep. 2007. doi: 10.1063/1.2773688

[15] D. B. Strukov *et al.*, "Exponential ionic drift: fast switching and low volatility of thin-film memristors," *Appl. Phys. A*, vol. 94, no. 3, pp. 515–519, Mar. 2009. doi: 10.1007/s00339-008-4975-3

[16] J. Tang *et al.*, "ECRAM as Scalable Synaptic Cell for High-Speed, Low-Power Neuromorphic Computing," in *2018 IEEE International Electron Devices Meeting (IEDM)*. San Francisco, CA: IEEE, Dec. 2018, pp. 13.1.1–13.1.4. doi: 10.1109/IEDM.2018.8614551

[17] H. Mehrer, *Diffusion in Solids*, ser. Springer Series in Solid-State Sciences, M. Cardona *et al.*, Eds. Berlin, Heidelberg: Springer Berlin Heidelberg, 2007, vol. 155.

[18] K. O. Geddes *et al.*, "Evaluation of classes of definite integrals involving elementary functions via differentiation of special functions," *AAECC*, vol. 1, no. 2, pp. 149–165, Sep. 1990. doi: 10.1007/BF01810298

[19] H. B. Fischer, *Mixing in Inland and Coastal Waters*. Elsevier, 1979.

[20] "COMSOL Multiphysics® v. 6.2. www.comsol.com. COMSOL AB, Stockholm, Sweden," Stockholm, Sweden.